Available online at www.sciencedirect.com
SCIENCE DIRECT®
Journal of Theoretical Biology 239 (2006) 33–48
Journal of Theoretical Biology
www.elsevier.com/locate/yjtbi

A numerical algorithm for investigating the role of the motor–cargo linkage in molecular motor-driven transport

John Fricks[a,1], Hongyun Wang[b], Timothy C. Elston[c,*]

[a]Department of Mathematics, University of North Carolina, Chapel Hill, NC 27599-3250, USA
[b]Department of Applied Mathematics and Statistics, University of California, Santa Cruz, CA 95064, USA
[c]Department of Pharmacology, University of North Carolina, Chapel Hill, NC 27599, USA

Received 23 March 2005; received in revised form 10 June 2005; accepted 18 July 2005
Available online 26 August 2005

Abstract

We extend the numerical algorithm developed by Wang et al. (2003. J. Theor. Biol. 221, 491–511) for studying biomolecular transport processes to include the linkage that connects molecular motors to their cargo. The new algorithm is used to investigate how the stiffness of the linkage affects the average velocity, effective diffusion coefficient, and randomness parameter. Three different models for molecular motors are considered: (1) a discrete stepping motor (2) a motor moving in a tilted-periodic potential and (3) a motor driven by a flashing potential. We demonstrate that a flexible motor–cargo linkage can make inferences on motor behavior based on measurements of the cargo's position difficult. We also show that even for the case of a tilted-periodic potential there exists an optimal stiffness of the linkage at which transport is maximized. The MATLAB code used in this paper is available at: http://www.unc.edu/~telston/code/.

Keywords: Molecular motors; Stochastic process; Markov chain; Numerical method

1. Introduction

The development of single-molecule techniques for measuring the biophysical properties of molecular motors has motivated the use of mathematical models to elucidate the mechanisms used by these proteins for force generation. Processive motors, such as kinesin, myosin, and dynein, are used for transporting vesicles within cells and for force generation during processes such as mitosis. In general, processive molecular motors consist of two head domains and move along microtubule or actin polymers. The heads interact with specific binding sites along the polymer track and are connected through α-helical coiled-coil stalk that extends from the neck region of each head. The stalk ends in a tail domain that is used to connect the motor to its cargo or to adjacent polymers.

There are three basic categories of models that are used to describe molecular motors. (See Julicher et al. (1997), Bustamante et al. (2001), Reimann (2002), Howard (1994) for reviews of molecular motors.) Spatially discrete models use continuous time Markov chains to describe the motion of the motor protein. The mathematical states of these models represent the different chemical states of the hydrolysis cycle used to drive the physical motion and the positions of the discrete binding sites along the polymer. While this approach can account for all the chemical steps in the reaction cycle, it does not model the physical motion of the free head as it moves between binding sites.

*Corresponding author. Department of Mathematics, University of North Carolina, Chapel Hill, NC 27599-3250, USA.
Tel.: +1 919 843 7670; fax: +1 919 966 5640.
E-mail addresses: fricks@stat.psu.edu (J. Fricks), hongwang@ams.ucsc.edu (H. Wang), telston@amath.unc.edu (T.C. Elston).
[1]Current address: Department of Statistics, Pennsylvania State University, University Park, PA 16802-2111, USA

0022-5193/$ - see front matter © 2005 Elsevier Ltd. All rights reserved.
doi:10.1016/j.jtbi.2005.07.010

Therefore, the approximation that underlies these models is that the continuous motion of the free head occurs instantaneously. Continuous models assume that the motor moves in a continuous free energy potential and is subject to thermal diffusion. These models more accurately represent the physical motion of the motor; however, they are only valid when the time-scale of the chemical kinetics is short as compared with the physical motion of the motor. The advantage of using fully discrete or continuous models is that they are analytically tractable and often provide qualitative insights into motor function. The third category of models treat changes in the chemical state of the motor as discrete events while maintaining the continuous motion of the heads. These models provide the most accurate description of the mechanochemistry that underlies energy transduction in molecular motors. Until recently most of the models of molecular motor function did not take into account the biophysical properties of the stalk region that connects the motor to its cargo. However, it is becoming increasingly clear that this linkage can have important consequences on the performance of the motor (Elston and Peskin, 2000; Elston et al., 2000; Xing et al., 2005; Chen and Yan, 2001; Chen et al., 2002).

Because of the small size of molecular motors, experiments are often performed by attaching a large bead to a single molecular motor and observing the motion of the bead. This experimental arrangement has the added advantage of allowing forces to be applied to the motor through the use of a laser trap. (See Visscher et al. (1999), Schnitzer et al. (1999), Block (1996), Maier et al. (2004), Hunt et al. (1994) for examples of experimental methods.) In this type of experimental arrangement, the underlying assumption is that the motion of the bead is representative of the motor's motion. While certainly true at a high level, if the tether between cargo and motor is not rigid but elastic, then the motor's motion is obscured, and inferences about the motor based on the beads behavior need to be made carefully. For example, Chen et al. (2002) demonstrated using a two-state discrete model with no reversible steps that the randomness parameter, which under appropriate assumptions is the reciprocal of the number of rate-limiting chemical steps, can deviate significantly from the expected value of $\frac{1}{2}$ when the motor–cargo linkage is elastic. Therefore, the empirically approximated randomness parameter cannot be trusted to infer the number of rate-limiting chemical steps per physical motor step. Another reason for considering the motor–cargo linkage is that the average velocity of the system depends on the properties of this connection. In fact, whether a flexible or stiff linkage produces more effective transport depends on the mechanism of force generation (Elston and Peskin, 2000; Elston et al., 2000).

Since rigorous analysis is complicated and generally restricted to asymptotic cases (e.g. the limits of infinitely stiff and weak springs) (Elston and Peskin, 2000; Elston et al., 2000), we suggest an extension of the numerical method proposed by Wang et al. (2003) (WPE) to include the cargo. In this method, the continuous spatial motion of the motor is described by an appropriate discrete approximation. The transition rates for the spatial motion are chosen so that the approximate discrete model converges to the continuous case in the limit that the grid size goes to zero. Additionally, the transition rates are chosen to preserve detailed balance for systems at equilibrium, a crucial feature required for accurately approximating asymptotic quantities. The numerical method is used to compute both the average velocity and effective diffusion coefficients. These asymptotic quantities can then be used to compute the randomness parameter. While Monte Carlo simulations could also be used to compute these quantities, our method has the advantage that no stochastic simulations are required. Therefore the error associated with finite sampling, which often dwarfs other sources of error such as discretization, is not an issue. In addition, we are interested in asymptotic quantities, and this method allows us to calculate these quantities without using a discretization in time. The numerical scheme presented here is well-suited for investigating intermediate spring constants that are not amenable to theoretical analysis. The models of molecular motors considered here have a spatially periodic structure that allows the motor's motion to be decomposed into transitions within a period and transitions between periods. The cargo does not have a periodic structure. However, the tether connecting the cargo to the motor keeps the cargo "near" the motor and thus requires us to calculate the distribution of the cargo only on a limited grid.

2. Model description and mathematical framework

Fig. 1 is a schematic diagram of a motor pulling a cargo. The state variables that describe this system are the position of the motor along the microtubule, x, the position of the cargo projected onto the microtubule, y, and the chemical state of the motor, i. In reality, the cargo is free to move in three dimensions. However, the dynamics of the motor are primarily along the direction of the microtubule, and we do not expect the qualitative behavior of this simplified system to deviate significantly from the true system (Elston and Peskin, 2000).

The equations of motion for this system are the following set of coupled Langevin equations:

$$\zeta_1 \frac{\mathrm{d}x}{\mathrm{d}t} = -\frac{\partial \Phi(x,y,i)}{\partial x} + \sqrt{2\zeta_1 k_B T} f_1(t), \tag{1}$$

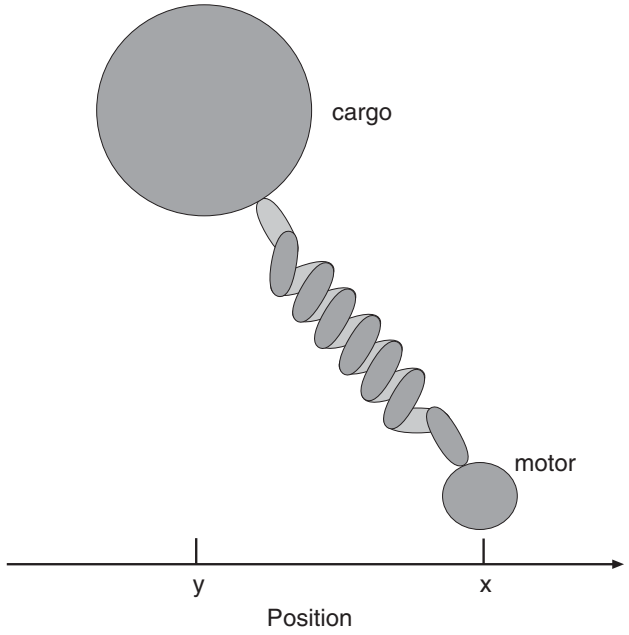

Fig. 1. A motor pulling cargo. The position of the motor along the track is given by x and the position of the cargo is y.

$$\zeta_2 \frac{\mathrm{d}y}{\mathrm{d}t} = -\frac{\partial \Phi(x,y,i)}{\partial y} + \sqrt{2\zeta_2 k_B T} f_2(t), \tag{2}$$

where $\Phi(x,y,i)$ is the potential energy of the system in chemical state i, ζ_1 and ζ_2 are the friction coefficients of the motor and cargo, respectively, $k_B T$ is the Boltzmann coefficient times the absolute temperature, and $f_1(t)$ and $f_2(t)$ are two independent Gaussian white-noise processes. The chemical state i is a random process whose behavior is described by a discrete space Markov chain. We restrict ourselves to a linear spring thus Φ has the form $\Phi(x,y,i) = (\kappa/2)(y-x)^2 + \phi_{tr}(x,i)$, where $\phi_{tr}(x,i)$ is the potential for the interaction between the motor and the track. The numerical algorithm presented here can handle more complicated potentials for the linkage including nonlinear and piecewise continuous, but the computational cost for these may be higher than for a quadratic potential.

The WPE method (Wang et al., 2003) only considered the motor (i.e. Eq. (1) with Φ replaced by ϕ_{tr}). Ignoring the chemical state of the motor, this leads to the following Fokker–Planck equation for the temporal and spatial evolution of the probability density

$$\frac{\partial \rho(x,t)}{\partial t} = D\frac{\partial}{\partial x}\left(\frac{1}{k_B T}\frac{\partial \phi_{tr}}{\partial x}\rho(x,t) + \frac{\partial}{\partial x}\rho(x,t)\right), \tag{3}$$

where $D = k_B T/\zeta$ is the diffusion coefficient. The force from the motor/track interaction, $-\partial\phi_{tr}/\partial x$, is assumed to be spatially periodic. Therefore, ϕ_{tr} is a tilted periodic potential. The WPE method depends on spatially discretizing the continuous process described by Eq. (3). In which case the Fokker–Planck equation may be approximated by the master equation for an approximating discrete process as follows (see appendix for details):

$$\frac{\mathrm{d}}{\mathrm{d}t}\mathbf{p}(j,t) = \mathbf{L}\mathbf{p}(j,t) + \mathbf{L}_+\mathbf{p}(j-1,t) + \mathbf{L}_-\mathbf{p}(j+1,t), \tag{4}$$

where

$$\mathbf{p}(j,t) = (p_1(j,t), p_2(j,t), \ldots, p_N(j,t))^{\mathrm{T}} \tag{5}$$

and $p_n(j,t)$ is the probability that the motor is at position $j\ell + (n-1)\ell/N$ at time t. That is, j denotes the period of the potential and n the position of the motor within the jth period which is divided into N grid points. The matrices $\mathbf{L}$, $\mathbf{L}_+$, and $\mathbf{L}_-$ contain the transitions within a period, the transitions to the following period, and the transitions to the previous period. Let F_n be the transition rate from site n forward to site $n+1$ and B_n the transition rate from site n backward to site $n-1$. The WPE method uses local solutions of Eq. (3) to calculate F_n and B_n as

$$B_n = \frac{D}{(\Delta x)^2}\cdot\frac{(-\Delta\phi_{n-1}/k_B T)}{\exp(-\Delta\phi_{n-1}/k_B T) - 1}, \tag{6}$$

$$F_n = \frac{D}{(\Delta x)^2}\cdot\frac{(\Delta\phi_n/k_B T)}{\exp(\Delta\phi_n/k_B T) - 1}, \tag{7}$$

where $\Delta\phi_n = \phi_{tr}(x_{n+1}) - \phi_{tr}(x_n)$. Matrices $\mathbf{L}$, $\mathbf{L}_+$, and $\mathbf{L}_-$ are sparse and consist of transition rates described above (see the appendix for details).

In this paper, we focus on computing three quantities that can be measured using single molecule techniques (Visscher et al., 1999; Schnitzer et al., 1999; Block, 1996): the average velocity, Vel, the effective diffusion coefficient, D_{eff}, and the randomness parameter, R. These three quantities are defined in the following way:

$$Vel \doteq \lim_{t\to\infty}\frac{E[X(t)]}{t}, \tag{8}$$

$$D_{eff} \doteq \lim_{t\to\infty}\frac{Var[X(t)]}{2t}, \tag{9}$$

$$R \doteq \frac{2D_{eff}}{\ell Vel}, \tag{10}$$

where ℓ is the length of the period of the potential, which corresponds to the step size of the motor. Because these quantities can be measured experimentally, any proposed model for energy transduction must faithfully capture their behavior under different experimental conditions. One advantage of the numerical method described above is that it provides a straightforward method for calculating the average velocity and effective diffusion equation without using Monte Carlo simulations. This is accomplished by using the following formulae derived by Wang et al. (2003) (see appendix for

more complete discussion):

$$Vel = \ell \sum_{n=1}^{N} [(\mathbf{L}_+ - \mathbf{L}_-)\mathbf{p}^s]_n, \tag{11}$$

$$D_{eff} = \frac{\ell^2}{2} \sum_{n=1}^{N} [(\mathbf{L}_+ + \mathbf{L}_-)\mathbf{p}^s + 2(\mathbf{L}_+ - \mathbf{L}_-)\mathbf{r}]_n, \tag{12}$$

where $\mathbf{p}^s$ and $\mathbf{r}$ are determined by

$$M\mathbf{p}^s = (\mathbf{L} + \mathbf{L}_+ + \mathbf{L}_-)\mathbf{p}^s = 0, \tag{13}$$

$$M\mathbf{r} = \left(\sum_{n=1}^{N} [(\mathbf{L}_+ - \mathbf{L}_-)\mathbf{p}^s]_n - (\mathbf{L}_+ - \mathbf{L}_-) \right) \mathbf{p}^s \tag{14}$$

subject to the constraints

$$\sum_{n=1}^{N} \mathbf{p}_n^s = 1, \tag{15}$$

$$\sum_{n=1}^{N} \mathbf{r}_n = 0. \tag{16}$$

It is important to point out that $\mathbf{p}^s$ and $\mathbf{r}$ are steady-state solutions. The calculation of average velocity and effective diffusion does not involve solving a time-dependent evolution. Note that because we have approximated the continuous processes as a Markov chain, it is also possible to use the analytic expressions derived by Kolomeisky and Fisher (2001, 2000a, b) to compute the average velocity and effective diffusion coefficient. However, the analytic expressions tend to become unwieldy quickly as the complexity of the system increases. Therefore it is simpler to solve Eqs. (11)–(16) numerically.

A common assumption is that the randomness parameter R is the reciprocal of the number of rate-limiting chemical steps that must occur for the motor to move forward one physical step. This is indeed true for the situation of a Markov jump process without reversible steps. For motors with an elastic linkage to a cargo, the randomness parameter is no longer a good indicator of how many internal substeps in one motor step (Chen and Yan, 2001). Additionally, this interpretation does not hold for reasonable alternative models, such as continuous space models (Wang et al., 2003). Nevertheless, the randomness parameter is related to the effective diffusion coefficient and is a constraint, in addition to the average velocity, on theoretical models. In comparing theoretical models with experimental results, it is important to compute the randomness parameter of the theoretical models accurately. Hence, it is important to have a reliable method for computing the randomness parameter that can be applied to all the different types of models.

As we show below, an important feature for generalizing the WPE method to the motor–cargo system is to consider the position of the cargo in terms of the distance from the last period crossed by the motor instead of its absolute position. When the motor moves into another period, the transition rates for the cargo are adjusted by the distance of one period. Thus, we are only required to track the position of the cargo on a finite grid covering a reasonable distance from the motor so that the probability of the cargo being outside this region is negligible. This description of the cargo position is critical for computing the effective diffusion coefficient. The details of the generalized algorithm are presented in the first example and in the appendix.

3. Examples

3.1. Two-state model

Chen et al. (2002) studied a simple model of a motor–cargo system in which the motor takes two substeps per period of the track. The substeps correspond to different chemical states of the motor. While this model does not fall into the formulation presented above for discretizing a continuous spatial model, it is a good example for demonstrating the numerical method. The motor is restricted to positions given by $x_{n,j} = \ell(j + (n-1)/2)$, where ℓ is the period length of the track (step size), j denotes the current period for the motor and n can either be 1 or 2 (see Fig. 2). Let $F^M(n)$ and $B^M(n)$ be the forward and backward transition rates

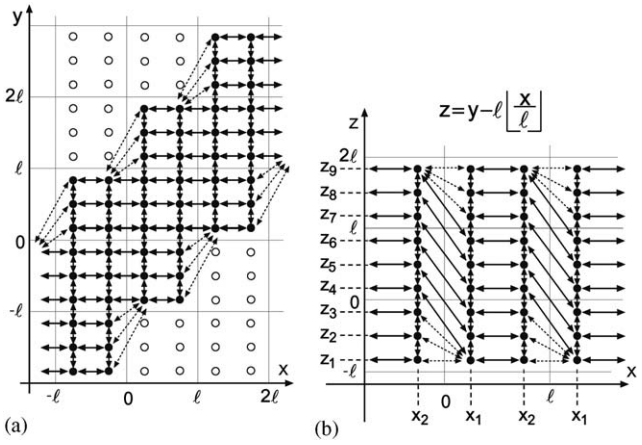

Fig. 2. Spatial discretization of the 2-D model for elastically coupled motor and cargo. (a) The left panel shows the discretization in x (coordinate of motor) and y (coordinate of cargo). Solid circles represent grid points used in computation. Hollow circles represent grid points not used in computation. Solid arrows represent the regular jumps that are derived from the differential equation. Dashed arrows represent ad hoc jumps that are added to better preserve the flow of probability when the computational domain of y is moderate. (b) The right panel shows the discretization in x and z where z is the distance between the cargo and the left edge of the period of x. We can see that as x jumps forward (backward) to the next period the computational domain of z stays the same and everything is period in x.

for the motor in the absence of the cargo. Note that $F^M(n)$ and $B^M(n)$ are independent of j and periodic in n (i.e. $F^M(n) = F^M(n+2)$ and $B^M(n) = B^M(n+2)$). Let the continuous variable $y(t)$ denote the position of the cargo at time t. To model the effects of the cargo, Chen et al. modified $F^M(n)$ and $B^M(n)$ in the following way:

$$F^M(n) \to F^M(j,n,y) = F^M(n)\mathrm{e}^{(-C_F(n)(\Delta\Phi_n(j,n,y))/k_BT)}, \quad (17)$$

$$B^M(n) \to B^M(j,n,y) = B^M(n)\mathrm{e}^{(C_B(n)(\Delta\Phi_n(j,n-1,y))/k_BT)}. \quad (18)$$

In the above equations the potential energy $\Phi(j,n,y) = (\kappa/2)(x_{n+1,j} - y)^2 + Fy$, where κ is the spring constant of the motor–cargo linkage, F is an experimentally applied load force, and $\Delta\Phi_n = \Phi(j,n+1,y) - \Phi(j,n,y)$. Following Chen et al. (2002), $C_F(n)$ is the fraction of the force from the linkage that affects forward movement when the motor moves from state n to $n+1$, and $C_B(n)$ is the fraction of the force from the linkage that affects backward movement when the motor moves from state n to $n-1$. Note that we have dropped the explicit time dependence of y and the conventions $x_{3,j} = x_{1,j+1}$ and $x_{0,j} = x_{2,j-1}$ are being used.

To use the numerical method presented above requires that the cargo's position be approximated as a discrete space random process. Let $y_m = m\Delta y$, where m can take on any integer value. The forward and backward transition rates for the cargo $B^C(j,n,m)$ and $F^C(j,n,m)$ are determined from Eqs. (6) and (7), respectively, using $\Delta\Phi_m = \Phi(j,n,m+1) - \Phi(j,n,m)$. We can see that for this problem the $\mathbf{L}$ matrix of Eq. (4) is invariant to translations by a distance ℓ. That is, in terms of the physical positions of the motor and cargo the following identity holds: $\mathbf{L}(x+\ell, y+\ell) = \mathbf{L}(x,y)$. (The $\mathbf{L}_\pm$ matrices also possess this symmetry.) However, to use Eqs. (11)–(16) for the average velocity and effective diffusion coefficient requires that the $\mathbf{L}$ matrices are invariant under the following operation $\mathbf{L}(x+\ell, z) = \mathbf{L}(x,z)$. That is, the matrices need to be invariant under translations of the motor alone. To achieve this symmetry, we introduced the variable z defined as the distance from the cargo to the left edge of the period that contains the motor. That is, $z_m = m\Delta y - \ell j$. For illustrative purposes, Fig. 2a shows the spatial discretization of the 2-D model for elastically coupled motor and cargo in x (motor coordinate) and y (cargo coordinate). For each period of x, the computational domain of y is finite. Solid circles represent grid points used in computation. Hollow circles represent grid points not used in computation. The computational domain of y does not change within a period of x. It is shifted up (down) when x goes forward (backward) to the next period. As discussed above, for clarity this example uses only two numerical grid points in one period $[0,\ell)$ in the x-direction. In the y-direction, we use three grid points in a length of size ℓ, and we use a computational domain of size 3ℓ for y. In actual computations of the 2-D model, the computational domain of y is determined by the value of the spring constant κ. For a soft spring (small value of κ), a large computational domain is needed to ensure the numerical accuracy. In Fig. 2a, solid arrows represent the regular jumps in the x or the y that are derived from the 2-D diffusion equation. Dashed arrows represent the boundary conditions for y. These are ad hoc jumps that are added to preserve the flow of probability and improve the computational accuracy when the computational domain of y is moderate. (See appendix for further details.) When the spring is stretched to a point where y would be beyond the computational domain, these jumps cause the cargo coordinate to remain at the boundary. When the computational domain of y is large, the probability of being near the ends of domain is small. Thus, the effect of these ad hoc jumps is insignificant when the computational domain is large enough. Fig. 2b shows the discretization in x and z coordinates, where z is the distance between the cargo and the left edge of the period of x. Mathematically,

$$z = y - \ell \cdot \left\lfloor \frac{x}{\ell} \right\rfloor,$$

where function $\lfloor\alpha\rfloor$ represents the largest integer that is less than or equal to α. It is clear that as x jumps forward (backward) to the next period the computational domain of z stays the same and everything is periodic in x. In the appendix, we give the explicit forms of the $\mathbf{L}$ matrices needed to implement the numerical scheme.

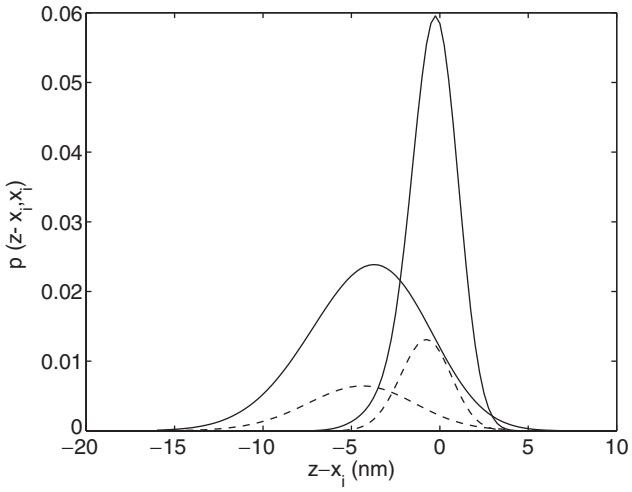

Fig. 3. Joint distributions for the motor and cargo. The curves on the left correspond to a spring constant of 8 pN/nm. The lower dashed curve is the function $p(z - x_1|x_1)p(x_1)$. That is, the joint density for the motor to be at position x_1 and the distance position of the cargo with respect to the motor to be $z - x_1$. The upper curve is the function $p(z - x_2|x_2)p(x_2)$. The curves on the right are the same except with a spring constant of 40 pN/nm. All four curves were calculated with $D = 300\,\mathrm{nm}^2/\mathrm{s} = 3 \times 10^{-12}\,\mathrm{cm}^2/\mathrm{s}$, $[ATP] = 2000\,\mu\mathrm{M}$, and $F = 0\,\mathrm{pN}$.

This example allows us to see in a simple framework some interesting aspects of the numerical method. Fig. 3 shows the stationary conditional distributions for the distance from the motor to the cargo $y - x$ and the motor position x. Each distribution is weighted by the probability for the motors position. That is, the curves represent $p(z - x_i, x_i) = p(z - x_i|x_i)p(x_i)$. Results for two different spring constants are presented. As expected, the distributions appear nearly Gaussian with the weaker spring producing greater variances. This type of plot gives a good diagnostic tool for determining the size and position of the grid required to accurately capture the distribution of the variable z. Additionally, we can sum over z to obtain the stationary distribution for the position of the motor. In this example, this would simply correspond to the probabilities for the motor to be at x_1 or x_2. Alternatively, we may sum over the probability of being in state x_1 and x_2 to obtain an unconditioned stationary distributions for z. (The distance from the cargo to the last period crossed by the motor.) We see such distributions in Fig. 4 which show the distribution of z for both a low and high spring constant.

The z variable can be used to provide information about the step distribution that would be measured from experiments in which a bead is attached to a motor protein (Block, 1996). Fig. 4 shows the distribution of z for two different spring constants. We can see that for a low spring constant the difference between steps is "washed out", and the distribution resembles a single Gaussian. A large spring constant more clearly displays a bimodal distribution confirming the fact that there are two substeps within each period. With a flexible linkage it would be very difficult to resolve substeps using a binning method. With a stiffer linkage it may be possible to identify substeps, although in practice this may still be difficult. Also note that the method presented here does not take into account the sampling rate. Therefore, while the method can give some indication of whether it is plausible to differentiate substeps, the effect of the stepping rate would need to be explored with a method which explicitly accounts for the dynamics of the motor, such as Monte Carlo simulations.

Fig. 5 shows the convergence of the effective diffusion coefficient as the grid size is reduced for varying spring constants. Fig. 6 is a log–log plot of the relative error in the effective diffusion coefficient as a function of the grid size. From this plot we see that the algorithm is second-order accurate in the grid size (Atkinson, 1989).

In the calculations that follow, we reproduce the results of Chen et al. (2002). For the dependence of the randomness parameter on the spring constant. In the absence of the cargo, the forward and backward rates for the motor are $F^M(1) = 3.75[ATP]$, $F^M(2) = 141.1$, $B^M(1) = 0.034$, and $B^M(2) = 0.0047$, where $[ATP]$ denotes the ATP concentration. The constants in the exponentials of Eqs. (17) and (18) are $C_F(1) = 0.25$, $C_B(1) = 0.435$, $C_F(2) = 0.065$, and $C_B(2) = 0.25$; these values are based on physical assumptions on how the force per step is distributed over the two substeps (Chen et al., 2002). The free parameters are then the spring constant κ, the diffusion coefficient of the cargo D, the ATP concentration $[ATP]$, and the applied force F. Figs. 7 and 8 show results for the randomness parameter as a function of the spring constant. The two figures correspond to different values for the cargo's diffusion coefficient. These curves show good agreement with the results presented in Figs. 5c and d of Chen et al. (2002).

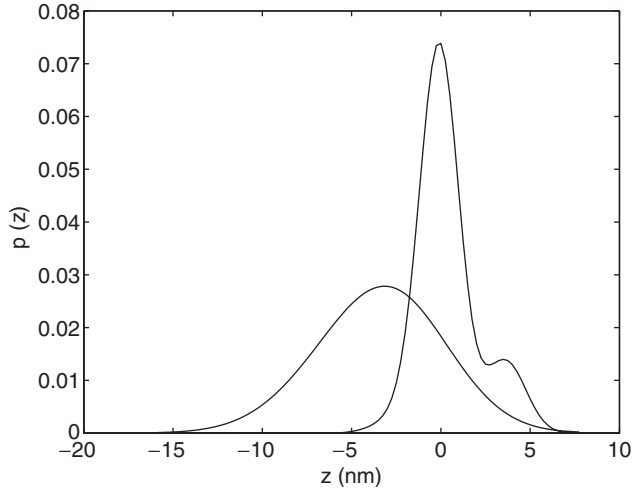

Fig. 4. Marginal distributions of $z = y - \ell\lfloor x/\ell \rfloor$. The curve on the left corresponds to a spring constant of 8 pN/nm. The curve on the right is the same except with a spring constant of 56 pN/nm. Both curves were calculated with $D = 300\,\mathrm{nm}^2/\mathrm{s} = 3 \times 10^{-12}\,\mathrm{cm}^2/\mathrm{s}$, $[ATP] = 2000\,\mu\mathrm{M}$, and $F = 0\,\mathrm{pN}$.

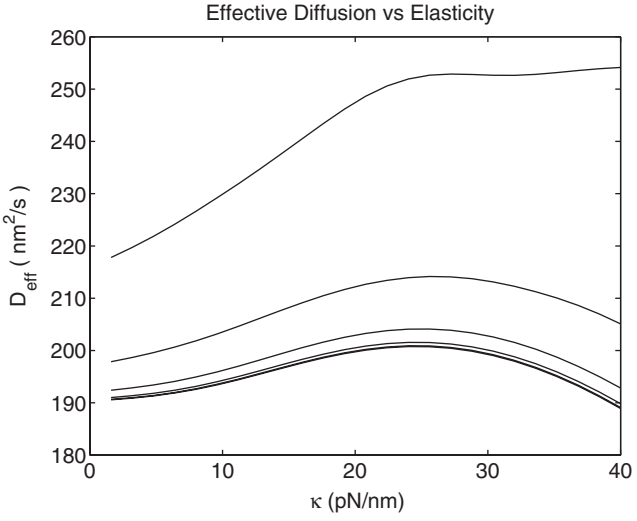

Fig. 5. Numerical convergence for the effective diffusion coefficient. In this figure $[ATP] = 20\,\mu\mathrm{M}$, $F = 0\,\mathrm{pN}$, and $D = 300\,\mathrm{nm}^2/\mathrm{s} = 3 \times 10^{-12}\,\mathrm{cm}^2/\mathrm{s}$. The curves from top to bottom correspond to $\Delta Y = 4, 2, 1, \frac{1}{2}, \frac{1}{4}, \frac{1}{8}$ nm.

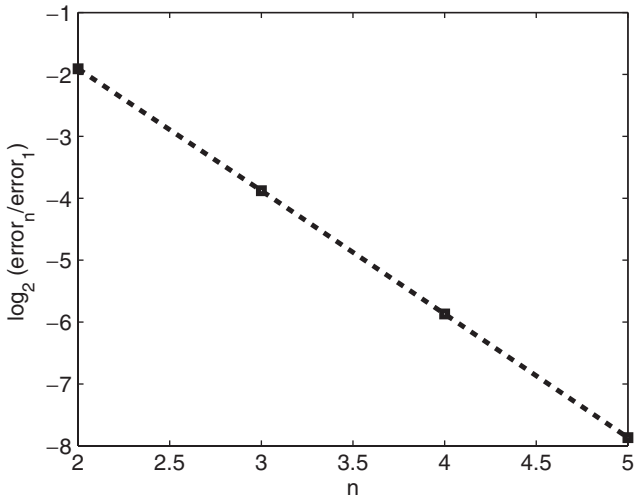

Fig. 6. Rate of convergence. $error_n = \langle D_{n+1}(\kappa) - D_n(\kappa) \rangle$ where $\langle \cdot \rangle$ is the L^1 norm and $D_n(\kappa)$ is the effective diffusion across values of κ (see Fig. 5) with $\Delta Y = 2^{3-n}$. A linear fit of the points has a slope of -1.98 showing second-order convergence.

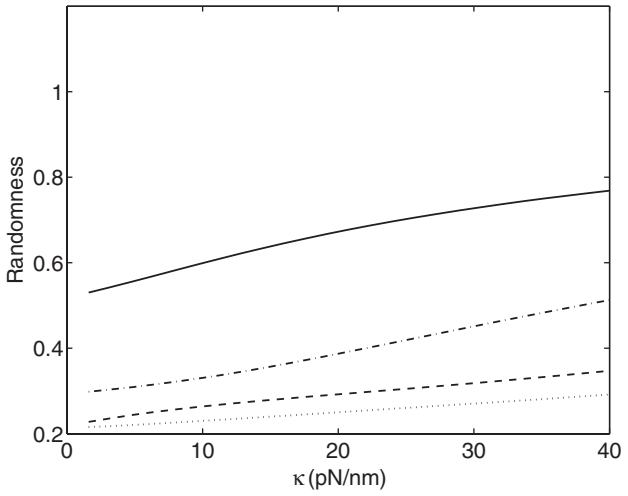

Fig. 8. Randomness parameter versus spring constant. This figure corresponds to Fig. 5d of Chen et al. (2002). This figure is the same as Fig. 7 except that the diffusion coefficient of the cargo equals $300\,\mathrm{nm}^2/\mathrm{s} = 3 \times 10^{-12}\,\mathrm{cm}^2/\mathrm{s}$.

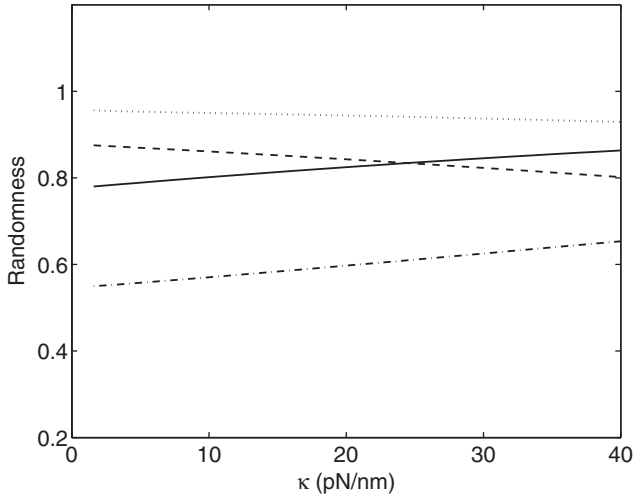

Fig. 7. Randomness parameter versus spring constant. This figure corresponds to Fig. 5c of Chen et al. (2002). The diffusion coefficient of the cargo equals $300,000\,\mathrm{nm}^2/\mathrm{s} = 3 \times 10^{-9}\,\mathrm{cm}^2/\mathrm{s}$. The dashdot line corresponds $[ATP] = 20\,\mu\mathrm{M}$ and $F = 0\,\mathrm{pN}$, the dotted line corresponds to $[ATP] = 2000\,\mu\mathrm{M}$ and $F = 0\,\mathrm{pN}$, the solid line corresponds to $[ATP] = 20\,\mu\mathrm{M}$ and $F = 3.59\,\mathrm{pN}$ and the dashed line corresponds to $[ATP] = 200\,\mu\mathrm{M}$ and $F = 3.59\,\mathrm{pN}$.

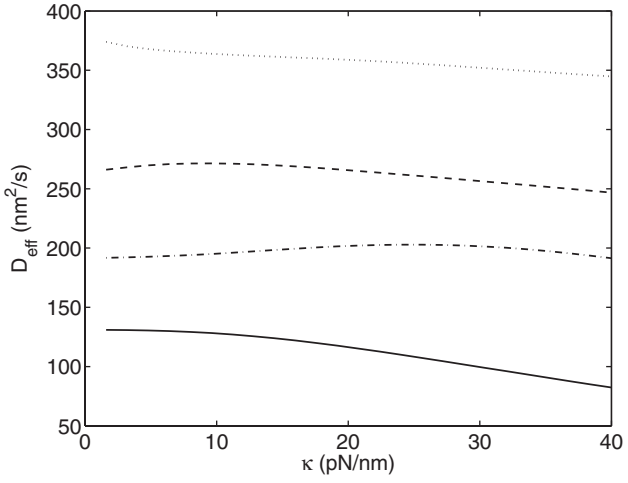

Fig. 9. Effective diffusion coefficient versus spring constant. The parameter values used to compute the curve shown in this figure are the same as in Fig. 8.

To obtain their results, Chen et al. developed a Monte Carlo method for simulating sample paths of the process and then averaged over many realizations. Therefore, the dominant source of error in their calculations is due to finite sampling in time. Unless very large sample sizes are used, which requires large amounts of computer time, these errors are significantly larger than the numerical errors that occur from finite grid effects. With our method we are able to resolve subtle trends that would not be easily observable using Monte Carlo methods. For example, the effective diffusion coefficient is seen to go through a local maximum in Fig. 9. Resolving this behavior using sample paths would be very computationally expensive.

A common interpretation of the randomness parameter is that it is the reciprocal of the number of rate-limiting chemical steps in the hydrolysis cycle that drives the motion of the motor. This interpretation is strictly correct in the absence of any cargo and when the chemical steps are irreversible. As pointed out by Chen et al. the randomness parameter can change significantly depending on the elastic properties of the tether connecting the motor and cargo. This is demonstrated in Fig. 8. This graph corresponds to a case in which the

diffusion coefficient of the cargo is considerably smaller than that of the motor (i.e. a large cargo). In each of the examples shown in this figure, the motor makes two chemical steps per physical step, and the forward rate constants are much larger than the backward ones. However, we can see that the randomness parameter can vary significantly from the value of $\frac{1}{2}$ expected for a system lacking cargo.

3.2. Tilted-periodic potential

Another class of models used to study molecular motors are those in which the motor moves in a titled-periodic potential. That is, the potential has the following property: $\phi_{tr}(x+\ell) = \phi_{tr}(x) - F\ell$, where the period length is ℓ and the average force per period is F. If $F = 0$ then the potential is periodic, and the motor does not experience a net velocity. In this example, we assume that the potential has the form of a tilted sine potential. The specific form of the potential for the motor–cargo system is

$$\Phi(x,y) = A\sin\left(\frac{2\pi}{\ell}x\right) - F\cdot x + \frac{\kappa}{2}(y-x)^2, \tag{19}$$

where A is the amplitude of the periodic part of the potential and κ is again the spring constant of the motor–cargo linkage. As discussed above, to implement the algorithm we must change variables from the position of the cargo, y, to the distance from the cargo to the left edge of the period that contains the motor, z.

Before presenting the numerical results, it is informative to consider the behavior of the system in various limits. Consider the limit in which $\kappa \to \infty$. In this case, the motor and cargo move as one object with a diffusion coefficient given by (Elston and Peskin, 2000),

$$D_{stiff} = \frac{D_x D_y}{D_x + D_y}. \tag{20}$$

The opposite limit in which $\kappa \to 0$ is a little more delicate. In this weak spring limit, the force felt by the motor as a result of the cargo is essentially constant (Elston and Peskin, 2000). Likewise, the cargo feels a constant force from the motor that is equal in magnitude but opposite in direction. This force balance along with the fact that the average velocity of the motor and cargo must be identical leads to a graphical method for determining the average velocity of the motor–cargo system in the weak spring limit (Elston and Peskin, 2000; Elston et al., 2000). This method is illustrated in Fig. 10. The figure shows a plot of the velocity of the motor as a function of a load force $-F_{load}$. Also shown is the average velocity of the cargo subject to a positive force F_{load} (i.e., the cargo velocity is F_{load}/ζ_2). The point at which the curves cross denotes the average velocity of the motor–cargo system. Let $-\tilde{F}$ denote the force at which the two curves cross.

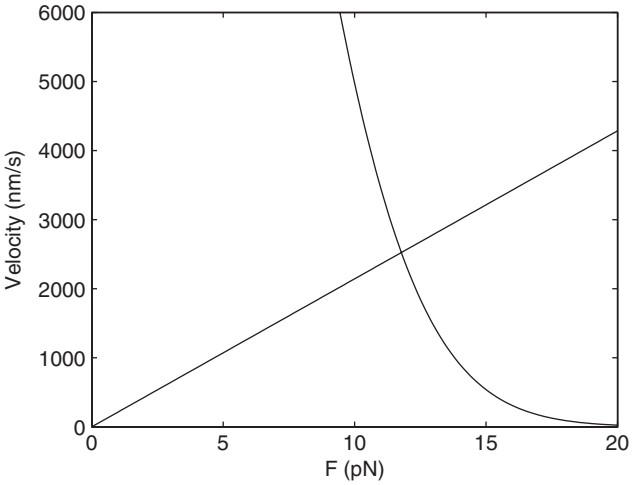

Fig. 10. Velocity versus load force. A positive force is applied to the cargo (increasing line) and a negative force is applied to the motor (decreasing curve). The point where the curves cross corresponds to the velocity of the motor–cargo system in the weak spring limit. The parameters for these curves are $A = 8k_BT$, $D_x = 9000\,\mathrm{nm}^2/\mathrm{s}$, $D_y = 900\,\mathrm{nm}^2/\mathrm{s}$, and $F = 30\,\mathrm{pN}$.

Using similar reasoning, the following formula for the effective diffusion coefficient can be derived (manuscript in preparation):

$$D_{weak} = \frac{(D_y/k_BT)^2 D_{eff}(F-\tilde{F}) + (V'(F-\tilde{F}))^2 D_y}{((D_y/k_BT) + V'(F-\tilde{F}))^2}, \tag{21}$$

where both $D_{eff}(F-\tilde{F})$ and $V(F-\tilde{F})$ can be calculated efficiently and accurately in 1-D simulations using the WPE method (Wang et al., 2003). Likewise, $V'(F-\tilde{F})$ is the derivative of the average velocity with respect to F under the same conditions. If in addition to the weak spring limit, we also consider the case in which $D_y/D_x \to 0$ (i.e., the motor diffusives very fast as compared to the cargo), then it is possible to show that the asymptotic velocity for the cargo is F/ζ_2 (Elston and Peskin, 2000). This represents an upper bound for the velocity of the motor–cargo system.

With these limiting behaviors in mind, we now use our numerical method to compute the average velocity and effective diffusion coefficient for different values of the spring constant κ. Fig. 11 is a plot of the average velocity versus κ for two different values of the motor diffusion coefficient D_x. In this figure $A = 8k_BT$, $\ell = 8\,\mathrm{nm}$ and $F = 30\,\mathrm{pN}$. The lower curve corresponds to a case in which the diffusion coefficient of the motor is 10 times larger than the diffusion coefficient of the cargo. The dashed horizontal lines represent the weak and stiff spring limits discussed above. There are two surprising features of this curve. First, the average velocity in the stiff spring limit is greater than that of the weak spring

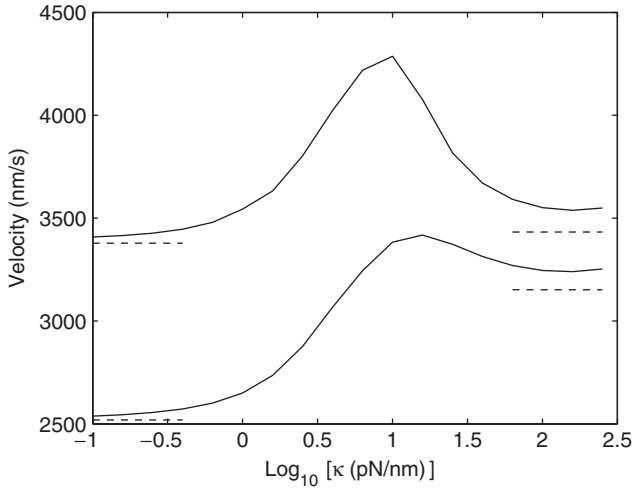

Fig. 11. Average velocity versus spring. The parameters for the lower curve are $A = 8k_BT$, $D_x = 9000\,\mathrm{nm}^2/\mathrm{s}$, $D_y = 900\,\mathrm{nm}^2/\mathrm{s}$, and $F = 30\,\mathrm{pN}$. The parameters for the upper curve are the same except for $D_x = 90,000\,\mathrm{nm}^2/\mathrm{s}$. The dashed lines correspond to the weak spring and tight spring limits.

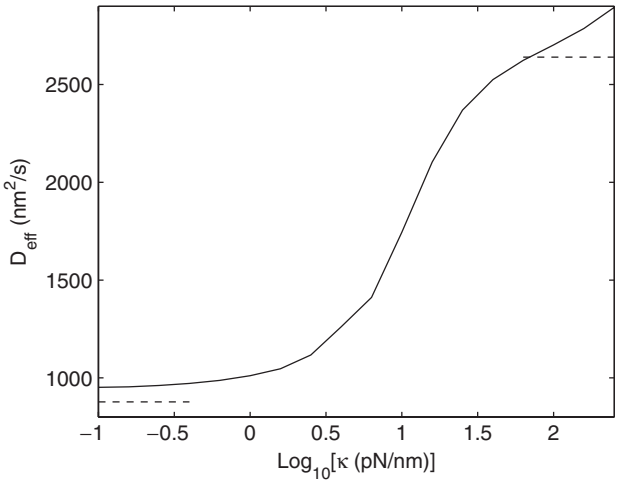

Fig. 12. Effective diffusion coefficient versus spring constant. The parameters for this curve are the same as in Fig. 11 with $D_x = 9000\,\mathrm{nm}^2/\mathrm{s}$. Again the dashed lines correspond to the weak and tight spring limits.

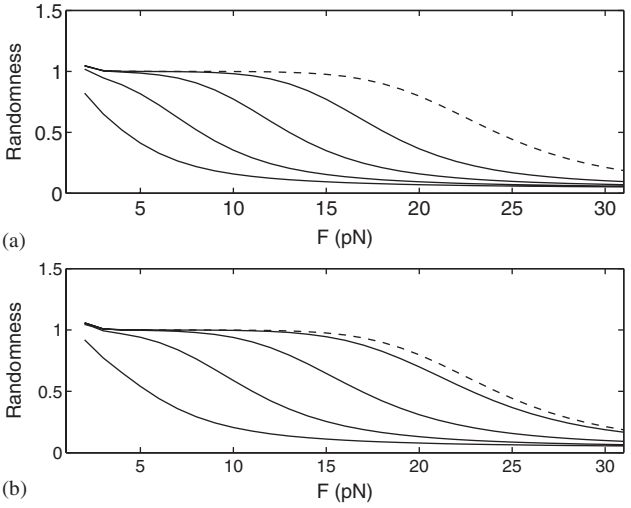

Fig. 13. Randomness versus force: (a) In this figure $\kappa = 6\,\mathrm{pN/nm}$. From left to right, the curves correspond to amplitudes of $2k_BT$, $4k_BT$, $6k_BT$, and $8k_BT$. The dashed curve corresponds to the stiff spring limit with an amplitude of $8k_BT$; (b) Same as in (a) except $\kappa = 10\,\mathrm{pN/nm}$.

limit, and second, the velocity goes through a maximum at a finite value of κ. This is in contrast to the results found by Elston and Peskin (2000) in which case the velocity was a monotonically decreasing value of the spring constant. The resolution to this apparent contradiction is that the average velocity computed by Elston and Peskin is an asymptotic result valid in the limit $D_y/D_x \to 0$. The upper curve in Fig. 11 corresponds to a case in which the diffusion coefficient of the motor is a hundred times greater than that of the cargo. As can be seen, the weak and stiff spring limits are now almost the same. If the diffusion coefficient of the cargo is further increased, the weak spring limit exceeds the stiff spring limit, and the curve becomes monotonically decreasing (data not shown). In this limit the weak spring asymptotic velocity is given by $F/\zeta_2 = 6.429\,\mathrm{nm/s}$, whereas the stiff spring asymptotic velocity is $3.466\,\mathrm{nm/s}$. The slow convergence of the weak spring limit to the asymptotic limit of F/ζ_2 is due to the large amplitude $A = 8k_BT$ of the potential. With this amplitude a very large motor diffusion coefficient is required to ensure that motor comes to a quasi-equilibrium with respect to the cargo. In contrast Elston and Peskin (2000) considered an imperfect ratchet and found that the asymptotic velocity was reached when $D_y/D_x = 0.01$. An important difference between the models is that in the tilted sine model, the motor must overcome a barrier to move to the next state, whereas in the ratchet model the barriers only prevent the motor from moving back to the previous state. Thus, the motor comes to quasi-equilibrium more rapidly in the ratchet model.

Fig. 12 shows the effective diffusion coefficient as a function of κ. Again, the horizontal dashed lines represent the weak and stiff spring limits. The weak spring limit was calculated from Eq. (21) and in the stiff spring limit D_{eff} is found by using the diffusion coefficient given in Eq. (20) in a system consisting of the motor alone moving in the tilted-sine potential. Note that for both the average velocity and the effective diffusion coefficient, there is considerable deviation from the asymptotic results and the numerical solutions in the large κ limit. This is due to numerical error that occurs as the transition rates become large. However, in the range of biologically realistic spring constants 0.5–25 pN/nm the algorithm works well.

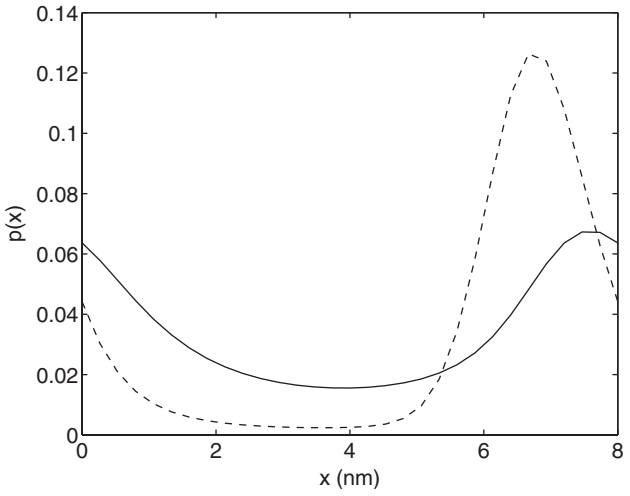

Fig. 14. Marginal stationary distribution for the position of the motor within a period. The dotted line corresponds to the motor with a moderately loose spring, $\kappa = 1\,\mathrm{pN/nm}$. The solid line corresponds to the tight spring limit. The parameters used in both curves are $A = 4k_BT$ and $F = 20\,\mathrm{pN}$.

Figs. 13a and b are plots of the randomness parameter as a function of F for various amplitudes A. In Fig. 13b, the spring constant $\kappa = 10\,\mathrm{pN/nm}$. In this case at large amplitudes, the randomness parameter remains near one for a wide range of forces and closely resembles the results of Wang et al. (2003) for a motor without a cargo. Therefore, the motor–cargo system is effectively behaving like a single particle, and in the region where the randomness parameter is near one, the system can be well approximated by a Poisson process. In contrast, in Fig. 13a, the spring constant has been reduced to 6 pN and the region over which the process looks Poisson is decreased. This result again highlights potential problems that can occur when making inferences about the motor's behavior from the motion of the cargo.

We have so far focused on asymptotic velocity and effective diffusion. However, our method can also be use to calculate the steady-state distributions for the motor and cargo. Fig. 14 shows the marginal probability distribution of the position of the motor. The solid curve represents the stiff spring limit. The dashed curve corresponds to a spring constant of 1 pN/nm. We can see that there is a considerable difference between the two distributions and that the distribution becomes sharper with a weaker spring.

3.3. Flashing ratchet

In general, the interaction between the motor and the polymer track along which it moves depends on the chemical state of the motor. Likewise, the reaction rates for the ATP hydrolysis cycle that drives the motion of the motor depend on the position and orientation of the motor on the track. This coupling of biochemical reactions with physical forces is referred to as mechanochemistry. Flashing ratchet models (also called correlation ratchets) provide a general mathematical framework for describing mechanochemistry and have been used to model many different types of molecular motors. In its simplest form, the flashing ratchet represents a Brownian particle whose dynamics is governed by a potential that can exist in two states. The transitions between the two configurations of the potential represent changes in the chemical state of the motor and therefore occur at random. For this simple model the Langevin equations for the motor and cargo are

$$\zeta_1 \frac{\mathrm{d}x}{\mathrm{d}t} = -\frac{\partial \Phi(x,y,i)}{\partial x} + \sqrt{2\zeta_1 k_B T} f_1(t), \tag{22}$$

$$\zeta_2 \frac{\mathrm{d}y}{\mathrm{d}t} = -\frac{\partial \Phi(x,y,i)}{\partial y} + \sqrt{2\zeta_2 k_B T} f_2(t), \tag{23}$$

where $i = 0, 1$ is a binary random variable that determines the state of the potential. A common choice for one state of the motor/track interaction is the sawtooth potential (Rousselet et al., 1994; Astumian, 1997; Peskin et al., 1994). In this state the potential for the motor–cargo system is given by

$$\Phi(x,y,1) = \frac{A}{p\ell}x + \frac{\kappa}{2}(y-x)^2 \quad \text{for } x \leqslant p\ell, \tag{24}$$

$$\Phi(x,y,1) = \frac{-A}{(1-p)\ell}(x-\ell) + \frac{\kappa}{2}(y-x)^2 \quad \text{for } x > p\ell, \tag{25}$$

where A is the amplitude of the sawtooth potential and p is a measure of the spatial asymmetry ($p = \frac{1}{2}$ for a symmetric potential). In the second state, we assume that the motor is free to diffuse along the track. That is, the full potential is given by

$$\Phi(x,y,0) = \frac{\kappa}{2}(y-x)^2. \tag{26}$$

The waiting time between transitions in the potential is assumed to be exponentially distributed and for simplicity independent of the motors position. To compute the average velocity and effective diffusion coefficient for this model requires a slight generalization of the method outlined above. The basic idea is to construct the matrices $\mathbf{L}$, $\mathbf{L}_+$, and $\mathbf{L}_-$ associated with each of the two potentials and also the matrices corresponding to transitions between the two states, then piece these matrices together to form large "$\mathbf{L}$" matrices for the full system.

Results for the average velocity and effective diffusion coefficient are shown in Fig. 15. In these plots the flashing rate increases from the top panel to the bottom panel. Again the dashed horizontal lines represent the

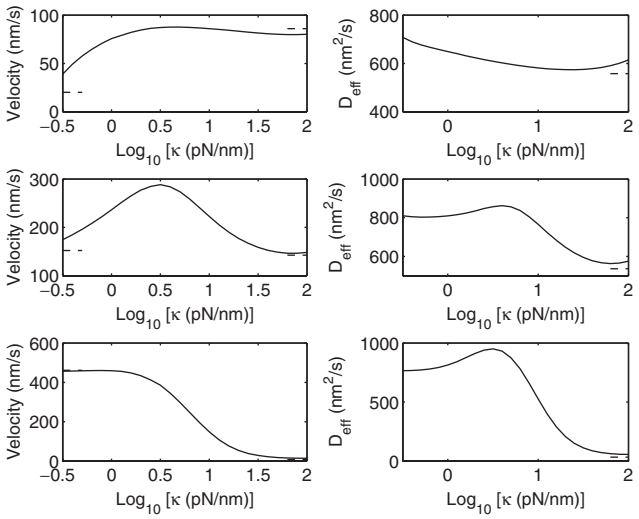

Fig. 15. Average velocity and effective diffusion coefficients versus spring constant. In each example, $A = 37.5k_BT$, $D_x = 9000\,\mathrm{nm}^2/\mathrm{s}$, and $D_y = 900\,\mathrm{nm}^2/\mathrm{s}$. The flashing rate is increasing from top to bottom. The top two figures correspond to a flashing rate of $10(D_y/\ell^2)$. The center two figures correspond to a flashing rate of $100(D_y/\ell^2)$. Finally the bottom figures have a flashing rate of $1000(D_y/\ell^2)$.

weak and stiff spring limits. The weak spring limit for the average velocity was computed in the same way as described above for the tilted-periodic potential. The stiff spring limits are computed using the motor alone with the diffusion coefficient given in Eq. (20). We have not attempted to calculate the weak spring limit of the effective diffusion coefficient. We can see that at the slowest flashing rate the average velocity starts at low and then reaches a slight maximum before leveling off at the stiff spring limit (top left panel). Again, the discrepancy between the asymptotic stiff spring limit and the numerical result is due to numerical error that arises when large spring constants are used in the transition rates. At intermediate flashing rates (middle left panel), the velocity is almost identical in the weak and stiff spring limits and goes through a pronounced maximum at intermediate values of the spring constant. In the limit of very fast flashing rates, the velocity is a monotonically decreasing function of the spring constant. These figures agree qualitatively with the results of Elston et al. (2000) obtained from Monte Carlo simulations. In that study, the authors also considered a two-state flashing ratchet. However, they used a smooth potential rather than the sawtooth potential used here. Results for the effective diffusion coefficient are shown in the right column. These results would be very difficult to obtain from Monte Carlo simulations, because this would require estimating the variance of the position at long times. In all three cases, the effective diffusion coefficient is larger in the weak spring limit than the stiff spring limit, and at moderate and fast switching rates it goes through a maximum value at intermediate values of the spring constant.

4. Discussion

We have expanded the numerical algorithm of Wang et al. (2003) for studying molecular motors to include the effect of the cargo. The important step in this generalization is to describe the system not in terms of the motor and cargo positions, but in terms of the motor position and the distance of the cargo to the left edge of the period of the track in which the motor is located. In addition to producing the steady-state probability distribution for the motor–cargo system, the algorithm can be used to directly calculate the randomness parameter, the effective diffusion coefficient, and the asymptotic velocity. Our method eliminates the need to average over multiple Monte Carlo simulations, which can be computationally expensive and inaccurate.

Several simple examples were used to show the important role that the cargo plays in determining the asymptotic properties of the motor. In the two-state stepping model, we verified the results of Chen et al. (2002) that illustrate that the randomness parameter of the motor–cargo system can strongly differ from the one predicted from the motor alone. Thus, inferences made about motor behavior based on measurements of the cargo should be done with care. For the example in which the motor moves in a tilted-sine potential, we discovered the surprising result that the average velocity depends non-monotonically on the stiffness of the motor–cargo linkage. We also found that depending on the ratio of the diffusion coefficients of the motor and cargo, the average velocity can be slower in the weak spring limit than in the stiff spring limit. This seems to contradict the results of Elston and Peskin (2000) in which it was shown that the velocity increases as the spring is weakened. However, this is an asymptotic result for the limit in which $D_y/D_x \to 0$. This limit requires that the motor comes to a quasi-equilibrium before the cargo moves a significant distance. The slow convergence to this limit seen here is due to the large amplitude of the sine potential which greatly increases the time required for the motor to come to equilibrium.

The numerical method seems to be quite successful over a broad range of parameter values and offers obvious advantages over Monte Carlo methods for calculating asymptotic quantities by eliminating errors that have accumulated in time and errors due to finite sampling. While the method outlined in the current work is not simulation based and has no time discretization, the method does produce numerical errors because it approximates a continuous state–space system as a discrete state–space process. These errors

lead to numerical instabilities at very large spring constants. This numerical error can be decreased by using the improved transition rates recently developed by Xing et al. (2005).

Mathematical models provide an important tool for understanding the mechanisms used by molecular motors for energy transduction. To compare these mathematical models with experimental data requires fast and accurate numerical techniques for analysing the models. For example, we discovered using our algorithm that for a motor–cargo system moving in a tilted sine potential there is an optimal spring constant at which the average velocity is maximized. This observation cannot be captured by analytical methods that are only valid in asymptotic limits or easily discovered by Monte Carlo simulations that require large amounts of computer time. The existence of such an optimal spring constant might help explain the biophysical properties of the linkage that connects molecular motors to their cargo.

Acknowledgements

J. Fricks was partially supported by National Science Foundation Post-doctoral Fellowship DMS-0403040. H. Wang was partially supported by NSF Grant DMS-0317937.

Appendix A. The WPE method

In this appendix, we review the WPE method proposed in Wang et al. (2003).

A.1. The WPE method for 1-D Fokker– Planck equations

We consider the 1-D Fokker–Planck equation

$$\frac{\partial \rho}{\partial t} = D\frac{\partial}{\partial x}\left(\frac{1}{k_B T}\frac{\partial \phi}{\partial x}\rho + \frac{\partial \rho}{\partial x}\right), \tag{27}$$

where $\phi(x)$ is a tilted periodic potential: $\phi(x+\ell) = \phi(x) - \Delta G$ and ℓ is the period.

We first divide the 1-D space $(-\infty, \infty)$ into a set of infinite number of periods of equal length ℓ. The jth period is defined as $[j\ell, (j+1)\ell)$. We further divide each period into a set of N subintervals of equal size $\Delta x = \ell/N$. Let us consider the local coordinate s of a numerical grid point within a period relative to the left boundary of the period. The nth numerical grid point in the jth period has local coordinate $s_n = (n-1)\Delta x$ and global coordinate $j\ell + s_n$. Thus, each numerical grid point is associated with a pair of indices (j, n), where j is the index of the period and n is the index of the grid point within that period. The global coordinate of grid point (j, n) is $j\ell + s_n$.

We use this infinite set of numerical grid points to represent the 1-D space $(-\infty, \infty)$. We discretize the continuous Markov process represented by the Fokker–Planck equation as a jump process on this infinite set grid points. Each numerical grid point represents a subinterval of size Δx centered at the grid point. The motor can jump from one grid point to an adjacent grid point (in the 1-D case, there are only two adjacent grid points).

Let $p_n(j,t)$ be the probability that the motor is at grid point (j, n) at time t. The evolution equation for $p_n(j,t)$ is

$$\begin{aligned}\frac{\mathrm{d}}{\mathrm{d}t}p_n(j,t) = &-(F_n + B_n)p_n(j,t) + F_{n-1}p_{n-1}(j,t)\\ &+ B_{n+1}p_{n+1}(j,t),\end{aligned} \tag{28}$$

where F_n is the rate of the motor jumping from grid point (j, n) to grid point $(j, n+1)$ and B_n is the rate of the motor jumping from grid point (j, n) to $(j, n-1)$. F_n and B_{n+1} are a pair of forward and backward jump rates between (j, n) and $(j, n+1)$. In Wang et al. (2003), the jump rates were derived by comparing the numerical probability flux with the exact probability flux corresponding to a local steady-state solution. F_n and B_{n+1} are given by

$$\begin{aligned}B_{n+1} &= \frac{D}{(\Delta x)^2}\cdot\frac{(-\Delta\phi_n/k_BT)}{\exp(-\Delta\phi_n/k_BT)-1},\\ F_n &= \frac{D}{(\Delta x)^2}\cdot\frac{(\Delta\phi_n/k_BT)}{\exp(\Delta\phi_n/k_BT)-1},\end{aligned} \tag{29}$$

where $\Delta\phi_n = \phi(s_{n+1}) - \phi(s_n)$. To calculate the jump rates between periods, we simply use the fact that the grid point $(j-1, N)$ is the same as $(j, 0)$, and the grid point $(j+1, 1)$ is the same as $(j, N+1)$. The behavior of the motor can be simulated using the evolution Eq. (28). For example, the average velocity of the motor is

$$V = \ell \lim_{t\to\infty}\frac{\sum_{j=-\infty}^{\infty}\sum_{n=1}^{N} j p_n(j,t)}{t}. \tag{30}$$

We can see that if we use Eq. (30) in a straightforward way to calculate the average velocity, we have to follow the dynamics of the motor over long time and over a very large computational domain. This is computationally very expensive. As we will see below, both the average velocity and the effective diffusion can be calculated from steady-state solutions (no time dependence) over just one period.

We put the probabilities at the N grid points of each period into a vector

$$\mathbf{p}(j,t) = (p_1(j,t), p_2(j,t), \ldots, p_N(j,t))^{\mathrm{T}}. \tag{31}$$

The evolution equation for $\mathbf{p}(j,t)$ is

$$\frac{\mathrm{d}}{\mathrm{d}t}\mathbf{p}(j,t) = \mathbf{L}\mathbf{p}(j,t) + \mathbf{L}_+\mathbf{p}(j-1,t) + \mathbf{L}_-\mathbf{p}(j+1,t). \tag{32}$$

In Eq. (28), $p_0(j,t) = p_N(j-1,t)$ and $p_{N+1}(j,t) = p_1(j+1,t)$. That is why, in Eq. (32), $\mathbf{p}(j,t)$ is affected by both $\mathbf{p}(j-1,t)$ and $\mathbf{p}(j+1,t)$. In Eq. (32), $\mathbf{L}$ is an $N \times N$ tridiagonal matrix with non-zero elements given by $\mathbf{L}_{n,n} = -(F_n + B_n)$,

$\mathbf{L}_{n-1,n} = B_n$,

$\mathbf{L}_{n+1,n} = F_n$,

$(\mathbf{L}_-)$ and $(\mathbf{L}_+)$ are two $N \times N$ matrices, each having only one non-zero element given by
$(\mathbf{L}_-)_{N,1} = B_1$,

$(\mathbf{L}_+)_{1,N} = F_N$.

In Eq. (32), $\mathbf{p}(j,t)$ has no steady-state solution. The motor position distribution will be further and further spread out. To express the average velocity in terms of a steady-state solution, we consider

$$\mathbf{p}(t) = (p_1(t), p_2(t), \ldots, p_N(t))^{\mathrm{T}} = \sum_{j=-\infty}^{\infty} \mathbf{p}(j,t), \tag{33}$$

$p_n(t)$ is the probability that the motor is at local grid point s_n (of some period) at time t. In Eq. (32), summing with respect to j, we obtain that $\mathbf{p}(t)$ satisfies

$$\frac{\mathrm{d}}{\mathrm{d}t}\mathbf{p}(t) = (\mathbf{L} + \mathbf{L}_+ + \mathbf{L}_-)\mathbf{p}(t), \tag{34}$$

$\mathbf{p}(t)$ does have a steady state. Let $\mathbf{p}^s$ be the steady state of $\mathbf{p}(t)$. $\mathbf{p}^s$ satisfies

$$(\mathbf{L} + \mathbf{L}_+ + \mathbf{L}_-)\mathbf{p}^s = 0 \tag{35}$$

subject to the constraint

$$\sum_{n=1}^{N} p_n^s = 1. \tag{36}$$

Now we express the average velocity in terms of $\mathbf{p}^s$. Multiplying Eq. (32) by vector $\mathbf{e} = (1, 1, \ldots, 1)$, we have

$$\frac{\mathrm{d}}{\mathrm{d}t}\left(\sum_{n=1}^{N} p_n(j,t)\right) = \mathbf{e}(\mathbf{L}_+(\mathbf{p}(j-1,t) - \mathbf{p}(j,t)) + \mathbf{L}_-(\mathbf{p}(j+1,t) - \mathbf{p}(j,t))). \tag{37}$$

Here we have used the fact that
$\mathbf{e}(\mathbf{L} + \mathbf{L}_+ + \mathbf{L}_-) = 0$.

Multiplying by j and summing with respect to j, we get

$$\begin{aligned}\frac{\mathrm{d}}{\mathrm{d}t}&\left(\sum_{j=-\infty}^{\infty}\sum_{n=1}^{N} j p_n(j,t)\right)\\ &= \mathbf{e}\left(\mathbf{L}_+ \sum_{j=-\infty}^{\infty} \mathbf{p}(j,t) - \mathbf{L}_- \sum_{j=-\infty}^{\infty} \mathbf{p}(j,t)\right)\\ &= \mathbf{e}(\mathbf{L}_+ - \mathbf{L}_-)\mathbf{p}(t)\\ &= \sum_{n=1}^{N} [(\mathbf{L}_+ - \mathbf{L}_-)\mathbf{p}(t)]_n,\end{aligned} \tag{38}$$

where $[\mathbf{u}]_n$ denotes the nth element of vector $\mathbf{u}$. Applying the L'Hôpital's rule to calculate the limit in Eq. (30), we obtain

$$V = \ell \sum_{n=1}^{N} [(\mathbf{L}_+ - \mathbf{L}_-)\mathbf{p}^s]_n. \tag{39}$$

To calculate the effective diffusion, we consider

$$\mathbf{r}(\mathbf{t}) = \sum_{j=-\infty}^{\infty}\left(j\mathbf{p}(j,t) - \mathbf{p}(j,t)\left[\mathbf{e}\sum_{j=-\infty}^{\infty} j\mathbf{p}(j,t)\right]\right), \tag{40}$$

$\mathbf{r}(t)$ has a steady state. Let $\mathbf{r}^s$ be the steady state of $\mathbf{r}(t)$. $\mathbf{r}^s$ satisfies (see Wang et al. (2003) for details of the derivation)

$$\begin{aligned}&(\mathbf{L} + \mathbf{L}_+ + \mathbf{L}_-)\mathbf{r}^s\\ &\quad = \left(\sum_{n=1}^{N} [(\mathbf{L}_+ - \mathbf{L}_-)\mathbf{p}^s]_n - (\mathbf{L}_+ - \mathbf{L}_-)\right)\mathbf{p}^s\end{aligned} \tag{41}$$

subject to the constraint

$$\sum_{n=1}^{N} r_n^s = 0. \tag{42}$$

Applying the L'Hôpital's rule to calculate the limit in

$$D_{eff} = \ell^2 \lim_{t\to\infty} \frac{\sum_{j=-\infty}^{\infty}\sum_{n=1}^{N} j^2 p_n(j,t) - (\sum_{j=-\infty}^{\infty}\sum_{n=1}^{N} j^2 p_n(j,t))^2}{2t},$$

we obtain

$$D_{eff} = \frac{\ell^2}{2}\sum_{n=1}^{N} [(\mathbf{L}_+ + \mathbf{L}_-)\mathbf{p}^s + 2(\mathbf{L}_+ - \mathbf{L}_-)\mathbf{r}^s]_n.$$

A.2. The WPE method for 2-D Fokker–Planck equations

We consider the 2-D Fokker–Planck equation

$$\begin{aligned}\frac{\partial\rho}{\partial t} &= D\frac{\partial}{\partial x}\left(\frac{1}{k_B T}\frac{\partial\Phi}{\partial x}\rho + \frac{\partial\rho}{\partial x}\right)\\ &\quad + D\frac{\partial}{\partial y}\left(\frac{1}{k_B T}\frac{\partial\Phi}{\partial y}\rho + \frac{\partial\rho}{\partial y}\right),\end{aligned} \tag{43}$$

where x represents the position of motor and y the position of cargo. The total potential is $\Phi(x,y) = \phi(x) + (\kappa/2)(y-x)^2$. Here $\phi(x)$ is a tilted periodic potential: $\phi(x+\ell) = \phi(x) - \Delta G$ with ℓ as the period, and $(\kappa/2)(y-x)^2$ is the elastic energy stored in the linkage connecting the motor and the cargo.

In the x-dimension, we divide $(-\infty, \infty)$ into a set of infinite number of periods of equal length ℓ. The jth period is $[j\ell, (j+1)\ell)$. We then divide each period into a set of N subintervals of equal size $\Delta x = \ell/N$. The local coordinate in the x-dimension of a numerical grid point within a period is defined as the distance from the left boundary of the period: $s = x - j\ell$. In the y-dimension the elastic potential increases quadratically as y getting away from x. So we can use a bounded computational domain. As the motor moves forward, the cargo will follow the motor. Therefore, the computational domain in the y-dimension needs to be changed from period to period. For the jth period, the motor position is between

$j\ell$ and $(j+1)\ell$. We use $[(j-y_0)\ell,(j+1+y_0)\ell]$ as the computational domain of y. For example, if $y_0=1$, then the computational domain of y for the zeroth period is $[-\ell,2\ell]$, and the computational domain of y for the first period is $[0,3\ell]$ as shown in Fig. 2. For the convenience of bookkeeping, we introduce a local coordinate in the y-dimension: $z=y-j\ell$. For z, the computational domain is always $[-y_0\ell,(1+y_0)\ell]$ as shown in Fig. 2. We divide $[-y_0\ell,(1+y_0)\ell]$ into M subintervals of equal size $\Delta y=((2y_0+1)\ell)/M$.

In this way, each grid point is associated with a triplet of indices (j,n,m) where $-\infty<j<\infty$ is the index of the period; $1\leqslant n\leqslant N$ is the index in the local coordinate $s=x-j\ell$; and $1\leqslant m\leqslant M+1$ is the index in the local coordinate $z=y-j\ell$. We use this infinite set of numerical grid points to represent the 2-D space of the motor–cargo system. We discretize the continuous Markov process represented by the Fokker–Planck equation as a jump process on this infinite set grid points. Each numerical grid point represents a subregion of size $(\Delta x)\times(\Delta y)$ centered at the grid point. The motor can jump from one grid point to another grid point adjacent to this one in the x coordinate or in the y coordinate.

The jump rates between grid points (j,n,m) and $(j,n,m+1)$ are given by Wang et al. (2003)

$$B^c_{n,m+1}=\frac{D_y}{(\Delta y)^2}\cdot\frac{(-\Delta_y\Phi_{n,m}/k_BT)}{\exp(-\Delta_y\Phi_{n,m}/k_BT)-1},$$
$$F^c_{n,m}=\frac{D_y}{(\Delta y)^2}\cdot\frac{(\Delta_y\Phi_{n,m}/k_BT)}{\exp(\Delta_y\Phi_{n,m}/k_BT)-1}, \tag{44}$$

where

$$\Delta_y\Phi_{n,m}=\Phi(s_n,z_{m+1})-\Phi(s_n,z_m)$$

and the script c denotes that these are the jump rates of the cargo. The jump rates between grid points (j,n,m) and $(j,n+1,m)$ are given by Wang et al. (2003)

$$B^m_{n+1,m}=\frac{D_x}{(\Delta x)^2}\cdot\frac{(-\Delta_x\Phi_{n,m}/k_BT)}{\exp(-\Delta_x\Phi_{n,m}/k_BT)-1},$$
$$F^m_{n,m}=\frac{D_x}{(\Delta x)^2}\cdot\frac{(\Delta_x\Phi_{n,m}/k_BT)}{\exp(\Delta_x\Phi_{n,m}/k_BT)-1}, \tag{45}$$

where

$$\Delta_x\Phi_{n,m}=\Phi(s_{n+1},z_m)-\Phi(s_n,z_m)$$

and the script m denotes that these are the jump rates of the motor. To calculate the jump rates between periods, we simply use the fact that grid point $(j+1,1,m)$ is the same as $(j,N+1,m+N)$, and grid point $(j-1,N,m)$ is the same as $(j,0,m-N)$.

Let $p_{n,m}(j,t)$ be the probability that the motor is at grid point (j,n,m) at time t. We put the probabilities at the $N\times(M+1)$ grid points of each period into a vector

$$\mathbf{p}(j,t)=\{p_{n,m}(j,t)\}. \tag{46}$$

The evolution equation for $\mathbf{p}(j,t)$ is

$$\frac{\mathrm{d}}{\mathrm{d}t}\mathbf{p}(j,t)=\mathbf{L}\mathbf{p}(j,t)+\mathbf{L}_+\mathbf{p}(j-1,t)+\mathbf{L}_-\mathbf{p}(j+1,t). \tag{47}$$

In Eq. (47), $\mathbf{L}$ is an $N\times N$ sparse matrix containing the jumps rates among the $N\times(M+1)$ grid points of the jth period; $\mathbf{L}_+$ contains the jump rates from the $(j-1)$th period to the jth period; and $\mathbf{L}_-$ contains the jump rates from the $(j+1)$th period to the jth period. $\mathbf{L}$, $\mathbf{L}_+$ and $\mathbf{L}_-$ always satisfy

$$\mathbf{e}(\mathbf{L}+\mathbf{L}_++\mathbf{L}_-)=0,\quad \mathbf{e}=(1,1,\ldots,1).$$

The average velocity is given in terms of a steady-state solution as

$$V=\ell\sum_{m=1}^{M+1}\sum_{n=1}^{N}[(\mathbf{L}_+-\mathbf{L}_-)\mathbf{p}^s]_{n,m}, \tag{48}$$

where the steady-state solution $\mathbf{p}^s$ satisfies the linear system

$$(\mathbf{L}+\mathbf{L}_++\mathbf{L}_-)\mathbf{p}^s=0 \tag{49}$$

subject to the constraint

$$\sum_{m=1}^{M+1}\sum_{n=1}^{N}p^s_{n,m}=1. \tag{50}$$

The effective diffusion is given by

$$D_{eff}=\frac{\ell^2}{2}\sum_{m=1}^{M+1}\sum_{n=1}^{N}[(\mathbf{L}_++\mathbf{L}_-)\mathbf{p}^s+2(\mathbf{L}_+-\mathbf{L}_-)\mathbf{r}^s]_{n,m},$$

where the steady-state solution $\mathbf{r}^s$ satisfies the linear system

$$(\mathbf{L}+\mathbf{L}_++\mathbf{L}_-)\mathbf{r}^s=\left(\sum_{m=1}^{M+1}\sum_{n=1}^{N}[(\mathbf{L}_+-\mathbf{L}_-)\mathbf{p}^s]_n-(\mathbf{L}_+-\mathbf{L}_-)\right)\mathbf{p}^s \tag{51}$$

subject to the constraint

$$\sum_{m=1}^{M+1}\sum_{n=1}^{N}r^s_n=0. \tag{52}$$

A.3. Example implementation

In this subsection, we provide further details on how to implement the numerical algorithm. In the previous subsection, we described the numerical grid designed for a motor–cargo system. Let $p_{n,m}(j,t)$ denote the probability that the motor–cargo system is at grid point (j,n,m) at time t. Here j is the index for the period that the motor is in, n is the index for the local coordinate of the motor relative to the left end of that period, and m is the index for the local coordinate of the cargo relative to the left end of that period. At the grid point (j,n,m), the motor position is $x=j\ell+s_n$ and the cargo position is $y=j\ell+z_m$. The biggest advantage of introducing local coordinates for motor and cargo within each period is

that both the computational domain and the indices for s_n and z_m are stationary going from one period to the next (see Fig. 2). The computational domain for the local coordinate of motor s_n is always $[0,\ell)$. In the example shown in Fig. 2, for clarity, we use 2 grid points for the local coordinate of motor $s_n : 1 \leqslant n \leqslant 2$.We select $[-\ell, 2\ell)$ as the computational domain for the local coordinate of cargo z_m. We use 9 grid points for $z_m : 1 \leqslant m \leqslant 9$. More specifically, the cargo's local coordinate is discretized into 9 states $\{z_1, z_2, \ldots, z_9\}$ with three states in the period ahead of the period that contains the motor ($\{z_9, z_8, z_7\}$), three in the period of the motor ($\{z_6, z_5, z_4\}$), and three in the period behind the motor ($\{z_3, z_2, z_1\}$). Define the vector $\mathbf{p}(j,t)$ in the following way:

$$\mathbf{p}(j,t) = (p_{1,1}(j,t), p_{2,1}(j,t), p_{1,2}(j,t), p_{2,2}(j,t), \ldots, p_{1,9}(j,t), p_{2,9}(j,t))^{\mathrm{T}}, \tag{53}$$

The important thing to recall is that as the motor moves forward one period, if the cargo remains at the same position, then the local coordinate of the cargo is shifted back one period. In the two-state model, we have only two grid points for the local coordinate of the motor: s_1 and s_2. To illustrate the transitions between periods, let us consider the case where the motor is at s_2 and the cargo is at z_j. When a transition moves the motor from s_2 of the current period to s_1 of the next period, the local coordinate of the cargo changes from z_j to z_{j-3} if $j-3 \geqslant 1$. For example, the system jumps from (s_2, z_5) to (s_1, z_2). If $j-3<1$, then, to conserve the probability, we let the local coordinate of the cargo changes to z_1 (see Fig. 2). For example, the system jumps from (s_2, z_2) to (s_1, z_1). The matrix $\mathbf{L}_+$ will therefore have the following form:

$$\begin{pmatrix}
0 & B^m(x_2,z_1) & 0 & B^m(x_2,z_2) & 0 & B^m(x_2,z_3) & 0 & B^m(x_2,z_4) & 0 & 0 & 0 & 0 & \ldots \\
0 & 0 & 0 & 0 & 0 & 0 & 0 & 0 & 0 & 0 & 0 & 0 & \ldots \\
0 & 0 & 0 & 0 & 0 & 0 & 0 & 0 & 0 & B^m(x_2,z_5) & 0 & 0 & \ldots \\
0 & 0 & 0 & 0 & 0 & 0 & 0 & 0 & 0 & 0 & 0 & 0 & \ldots \\
0 & 0 & 0 & 0 & 0 & 0 & 0 & 0 & 0 & 0 & 0 & B^m(x_2,z_6) & \ldots \\
0 & 0 & 0 & 0 & 0 & 0 & 0 & 0 & 0 & 0 & 0 & 0 & \ldots \\
0 & 0 & 0 & 0 & 0 & 0 & 0 & 0 & 0 & 0 & 0 & 0 & \ldots \\
\ldots & \ldots & \ldots & \ldots & \ldots & \ldots & \ldots & \ldots & \ldots & \ldots & \ldots & \ldots &
\end{pmatrix}.$$

$\mathbf{p}(j,t)$ is a vector with 18 components. It evolves according to Eq. (4). The matrix $\mathbf{L}$ is now an 18×18 matrix with the form

$$\begin{pmatrix}
-\Sigma_1 & B^m(s_2,z_1) & B^c(s_1,z_2) & 0 & 0 & 0 & \ldots \\
F^m(s_1,z_1) & -\Sigma_2 & 0 & B^c(s_2,z_2) & 0 & 0 & \ldots \\
F^c(s_1,z_1) & 0 & -\Sigma_3 & B^m(s_2,z_2) & B^c(s_1,z_3) & 0 & \ldots \\
0 & F^c(s_2,z_1) & F^m(s_1,z_2) & -\Sigma_4 & 0 & B^c(s_2,z_3) & \ldots \\
0 & 0 & F^c(s_1,z_2) & 0 & -\Sigma_5 & B^m(s_2,z_3) & \ldots \\
\ldots & \ldots & \ldots & \ldots & \ldots & \ldots & \ldots
\end{pmatrix},$$

where $\Sigma_i = \sum_{j \neq i} (\mathbf{L} + \mathbf{L}_- + \mathbf{L}_+)_{i,j}$. $F^m(s_i, z_j)$ is the forward rate for the motor when the motor is at local coordinate s_i and the cargo is at local coordinate z_j. Similarly, $B^m(s_i, z_j)$ is the backward rate for the motor, and $F^c(s_j, z_i)$ and $B^c(s_j, z_i)$ are the forward and backward rates for the cargo. These rates are given in Eqs. (44) and (45).

Now, let us look at one of the matrices representing the transitions from one period to the next, namely $\mathbf{L}_+$. A similar procedure must be carried out when creating the matrix $\mathbf{L}_-$.

References

Astumian, R.D., 1997. Thermodynamics and kinetics of a brownian motor. Science 276, 917–922.

Atkinson, K.E.E., 1989. Introduction to Numerical Analysis. Wiley, New York.

Block, S., 1996. Fifty ways to love your lever: myosin motors. Cell 87, 151–157.

Bustamante, C., Keller, D., Oster, G., 2001. The physics of molecular motors. Acc. Chem. Res. 34, 412–420.

Chen, Y.-D., Yan, B., 2001. Theoretical formalism for bead movement powered by single two-headed motors in a motility assay. Biophys. Chem. 91, 79–91.

Chen, Y.-D., Yan, B., Rubin, R.J., 2002. Fluctuations and randomness of movement of the bead powered by a single kinesin molecule in a force-clamped motility assay: Monte Carlo simulations. Biophys. J. 83, 2360–2369.

Elston, T.C., Peskin, C.S., 2000. The role of protein flexibility in molecular motor function: coupled diffusion in a tilted periodic potential. SIAM J. Appl. Math. 60 (3), 842–867.

Elston, T.C., You, D., Peskin, C.S., 2000. Protein flexibility and the correlation ratchet. SIAM J. Appl. Math. 61 (3), 776–791.

Howard, J., 1994. Mechanics of Motor Proteins and the Cytoskeleton. Sinauer, Sunderland, MA.

Hunt, A.J., Gittes, F., Howard, J., 1994. The force exerted by a single kinesin molecule against a viscous load. Biophys. J. 67, 766–781.

Julicher, F., Ajdari, A., Prost, J., 1997. Modeling molecular motors. Rev. Mod. Phys. 69 (4), 917–922.

Kolomeisky, A.B., Fisher, M.E., 2000a. Extended kinetic models with waiting-time distributions: exact results. J. Chem. Phys. 113, 10867–10877.

Kolomeisky, A.B., Fisher, M.E., 2000b. Periodic sequential kinetic models with jumping, branching, and deaths. Physica A 279 (1–4), 1–20.

Kolomeisky, A.B., Fisher, M.E., 2001. Exact results for parallel-chain kinetic models of biological transport. J. Chem. Phys. 115, 7253–7259.

Maier, B., Koomey, M., Sheetz, M., 2004. A force-dependent switch reverses type iv pilus retraction. Proc. Natl Acad. Sci. 101 (31), 10961–10966.

Peskin, C., Ermentrout, B., Oster, G., 1994. Cell Mechanics and Cellular Engineering. Springer, New York, NY.

Reimann, P., 2002. Brownian motors: noisy transport far from equilibrium. Phys. Rep. 361, 57–265.

Rousselet, J., Salome, L., Ajdari, A., Prost, J., 1994. Directional motion of brownian particles induced by a periodic asymmetric potential. Nature 370, 446–448.

Schnitzer, M., Visscher, K., Block, S., 1999. Force production by single kinesin motors. Nat. Cell Biol. 2, 718–723.

Visscher, K., Schnitzer, M., Block, S., 1999. Single kinesin molecules studied with a molecular force clamp. Nature 400, 184–189.

Wang, H., Peskin, C.S., Elston, T.C., 2003. A robust numerical algorithm for studying biomolecular transport processes. J. Theor. Biol. 221, 491–511.

Xing, J., Wang, H., Oster, G., 2005. From continuum Fokker–Planck models to discrete kinetic models. Biophys. J., in press.